A TRANSIENT NUMERICAL MODEL FOR SENSIBLE FIXED-BED REGENERATOR IN HVAC APPLICATIONS

Hadi Ramin[a*], Easwaran N. Krishnan[a], A. Gurubalan[a], Wahab O. Alabi[a], Carey J. Simonson[a]

[a]Department of Mechanical Engineering, University of Saskatchewan,57 Campus Drive, Saskatoon, SK S7N 5A9, Canada

[*]**Corresponding author**: Hadi Ramin, hadi.ramin@usask.ca

A TRANSIENT NUMERICAL MODEL FOR SENSIBLE FIXED-BED REGENERATOR IN HVAC APPLICATIONS

ABSTRACT

Fixed-bed regenerators (FBRs) are energy recovery exchangers that can significantly reduce the energy required to condition outdoor ventilation air in HVAC systems. FBRs have high sensible effectiveness but produce an outlet air temperature that varies with time. In this paper, a numerical model is developed to evaluate the performance of FBRs, and more specifically, the transient nature of their operation. This transient nature poses difficulties for experimental testing; thus, the developed model consists of an exchanger (FBR) model and a sensor model to differentiate the actual exchanger performance from the performance that would be measured in an experiment. The developed numerical model is validated with experimental data and correlations from the literature. The numerical model is capable of capturing the transient behavior of FBRs and temperature sensors to accurately predict the measurement errors that can occur due to the transient response characteristics of FBRs and sensors at different operating conditions in HVAC applications.

Keywords: Transient numerical model; Temperature measurement; Performance testing; Sensible effectiveness; Heat recovery; Sensor transient response, test standards (ASHRAE standard 84 and CSA C439-18 standard).

Nomenclature

A_g	cross-sectional area of the airflow duct, m^2	P_h	heating period, s
A_m	matrix cross-sectional area, m^2	Pr	Prandtl number
$A_{m,c}$	matrix cold side cross-sectional area, m^2	T_g	airstream temperature, °C
$A_{m,h}$	matrix hot side cross-sectional area, m^2	$T_{c,i}$	cold airstream inlet temperature, °C
$A_{m,t}$	total hot and cold sides matrix cross-sectional area, m^2	$T_{c,o}$	cold airstream outlet temperature, °C
A_s	heat transfer surface area of exchanger channel, m^2	$\bar{T}_{c,o}$	time-averaged cold airstream outlet temperature, °C
A_{ts}	heat transfer surface area of sensor, m^2	$T_{h,i}$	hot airstream inlet temperature, °C
C^*	heat capacity rate ratio	$T_{h,o}$	hot airstream outlet temperature, °C
Cp_m	specific heat capacity of matrix, J/(kg·K)	$\bar{T}_{h,o}$	time-averaged hot airstream outlet temperature, °C
Cp_g	specific heat capacity of air, J/(kg·K)	$T_{initial}$	initial temperature, °C
Cp_{ts}	specific heat capacity of sensor, J/(kg·K)	T_m	matrix temperature, °C
Cr^*	matrix heat capacity ratio	T_s	sensor temperature, °C
D_h	hydraulic diameter, m	t	time, s
h	convective heat transfer coefficient, $W/(m^2 \cdot K)$	V	mean airflow velocity, m/s
h_c	channel height, m	V_{NS}	airflow velocity corresponding to non-instantaneous movement of exchanger, m/s
$(hA_s)^*$	convective conductance ratio	V_{ts}	volume of temperature sensor, m^3
i,j,k, m	integers	W	width of the exchanger, m
k_g	thermal conductivity of air, W/(m·K)	x	axial coordinate, m
k_m	thermal conductivity of matrix, W/(m·K)	x^*	dimensionless axial distance ($x/D_h \cdot Re \cdot Pr$)
L	length of the heat exchanger, m	**GREEK SYMBOLS**	
max	maximum	$\Delta\varepsilon$	Effectiveness error due to transient characteristic of temperature sensor (%)
min	minimum	α^*	rectangular aspect ratio
$\dot{m}_c$	cold stream mass flow rate, kg/s	ε	effectiveness (%)
$\dot{m}_h$	hot stream mass flow rate, kg/s	ρ_g	air density, kg/m^3
$(\dot{m}C_p)_h$	hot stream heat capacity rate, W/K	ρ_m	matrix density, kg/m^3
$(\dot{m}C_p)_c$	cold stream heat capacity rate, W/K	ρ_{ts}	temperature sensor density, kg/m^3
n	number of middle channels in exchanger	τ_s	sensor time constant, s
N_s	number of spatial nodes	λ	conduction parameter
NTU_o	overall number of transfer units	**ACRONYMS**	
Nu	Nusselt number	AAEE	Air to Air Energy Exchanger
Nu_{FD}	fully-developed Nusselt number	EX	Exchanger
Nu^*	normalized Nusselt number, Nu/Nu_{FD}	FBR	Fixed-Bed Regenerator
P	total cycle time, s	HVAC	Heating, Ventilating and Air Conditioning
Re	Reynolds number		
P_c	cooling period, s		

1 Introduction

In recent decades, air infiltration and energy losses through the envelope of buildings have decreased significantly through increased thermal resistance and building airtightness. As such, modern buildings are more isolated from the outside, which leads to a greater need for fresh outdoor air and high energy demand for ventilation to maintain the required indoor air quality [1]. Furthermore, as other energy losses from buildings are reduced, the fraction of energy needed for ventilation air increases. A common way to reduce the energy requirement for conditioning ventilation air is to incorporate air-to-air energy exchangers (AAEEs) into building heating, ventilating, and air conditioning (HVAC) systems to recover energy from the exhaust air as shown in Fig. 1 [2]. In terms of energy exchange, AAEEs are broadly classified into recuperative and regenerative exchangers. In recuperative exchangers, the hot and cold airstreams flow through separate channels within the exchanger. However, in regenerators (shown in Fig. 2 (a) &(b)), the hot and cold fluids flow through the same channels intermittently. The heat from the hot fluid is stored in the exchanger matrix (heating period), which is then released to the cold fluid during subsequent exposure of the exchanger to the cold fluid (cooling period) (as shown Fig. 2 (a) &(b)) [3].

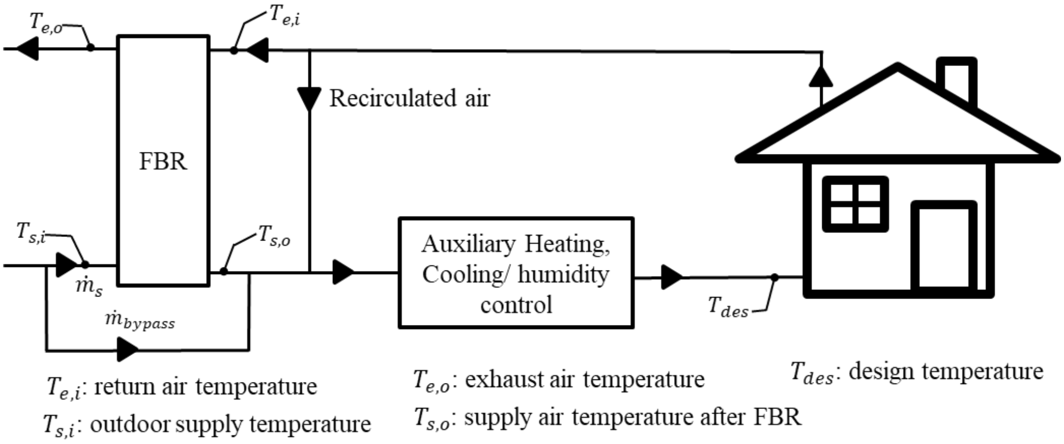

Figure 1. A schematic of an HVAC system with FBRs for heat recovery

Rotary regenerators (energy wheels) and fixed-bed regenerators (FBRs) are two types of regenerators. Energy wheels rotate cyclically between hot and cold airstreams for continuous operation, while dampers alternate the airflow through stationary matrixes in FBRs. The rotary regenerators' typical rotational speed is 0.5-3 rpm for power plants and 0.5-20 rpm for HVAC applications [4]. Energy wheels have been extensively studied for energy recovery in HVAC applications [2,5–9], and FBRs have been used for heat recovery in high-temperature applications such as glass furnaces, coke ovens, and open-hearth steel furnaces [10–13]. In recent times, FBRs have been attracting increasing attention for energy recovery in HVAC applications due to their high effectiveness [1,14–18]. Typical heating and cooling periods of FBRs are about 20 minutes for glass furnace applications [12,13], whereas, in the HVAC industry, a shorter period duration of 15-120 seconds is required [18–20].

(a) Heating period

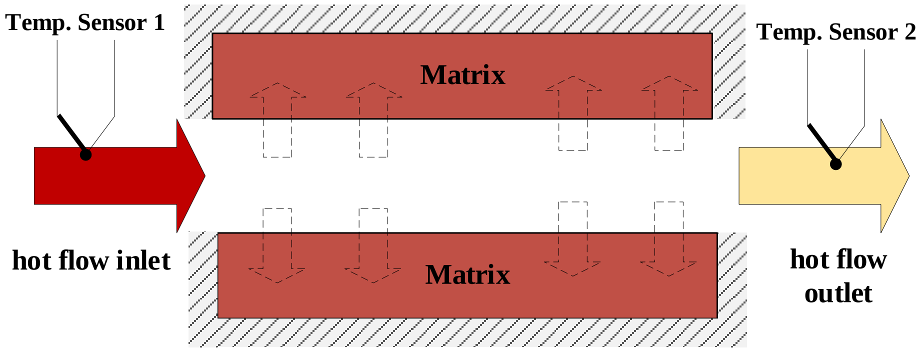

(b) Cooling period

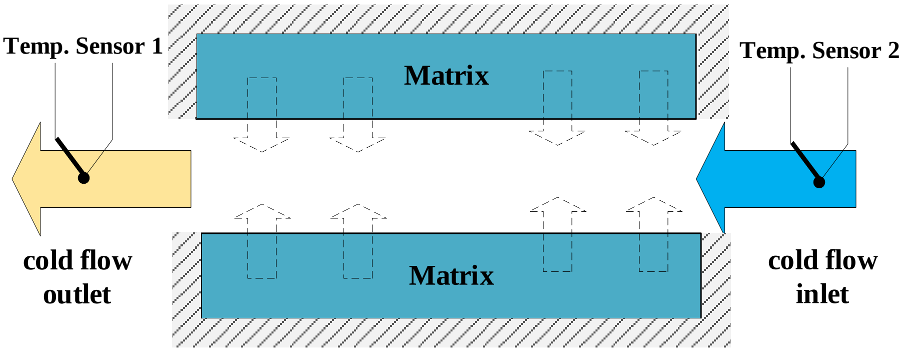

(c) Sensor temperature exposure

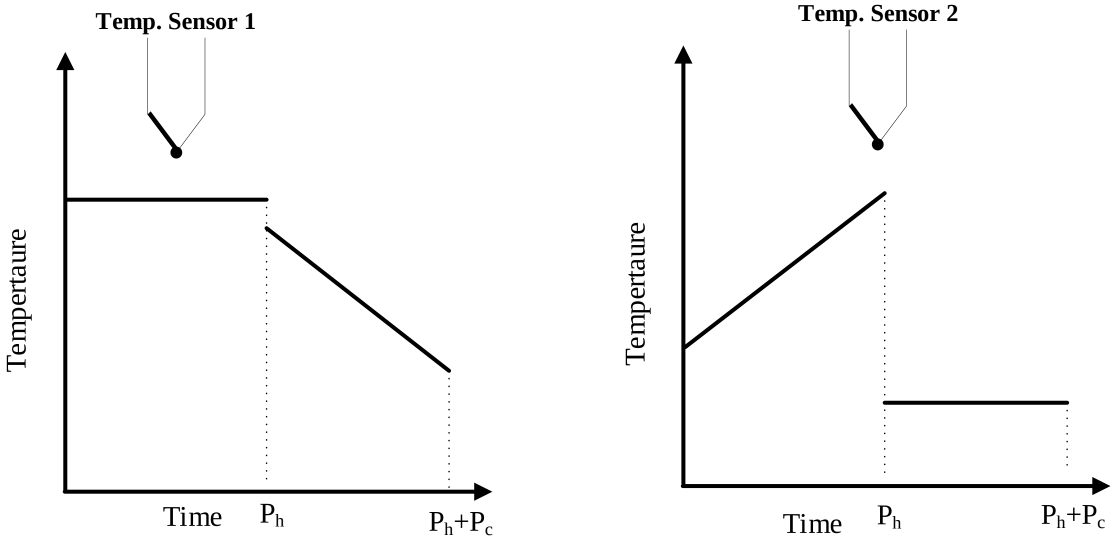

Figure 2: Schematic of alternate heating and cooling processes of FBRs and the corresponding temperature profile for temperature measurement sensors

The same governing equations govern the heat transfer process of FBRs as that of energy wheels [21,22]. But in contrast to energy wheels and recuperative exchangers, FBRs never attain a steady-state condition; instead, FBRs reach a periodic steady-state where the outlet air temperature changes during each period but is repeated from period to period. Furthermore, due to switching between the hot and cold flows, the temperature measured at the outlet (of FBR) at the beginning of each period is affected by the temperature that sensor was exposed to during the previous period (as shown in Fig.2 (c)) because of the thermal mass of the sensor [20,23,24]. Although models were available for FBRs in high-temperature applications since 1950 [22,25], the transient region was negligible for those applications because of the extended heating/cooling period (20 minutes). Krishnan et al. [20] reported significant deviations in the experimental determination of the effectiveness of FBRs due to sensor transient, especially at the shorter operating cycles (15 seconds). In recent studies of FBRs for HVAC applications [1,16,18], the mathematical models have been used to predict the effectiveness, but the initial transient region has not been explored. Overall, the model and analysis of this transient behavior of FBRs coupled with temperature measurement sensors are not in the current literature, which is the research gap this paper addresses.

A detailed numerical model to evaluate the sensible effectiveness and analyze the transient nature of the outlet air temperature of FBRs is developed. The developed numerical model consists of an exchanger (FBR) model and a sensor model. The exchanger model captures the transient behavior of the outlet temperature profile of FBRs, while the sensor model predicts the temperature recorded by the temperature measurement sensors. This paper elucidates the significance of transient temperature measurements in FBRs, and the effect of transient temperature measurement for operating conditions of balanced/unbalanced flow rate, as well as equal/unequal heating/cooling periods.

2 Numerical model for the FBR and temperature sensor

2.1 Exchanger (FBR) Model

Exchangers consist of many small channels that air flows through them intermittently. Numerical models are usually performed on a representative channel since all the channels have similar flow and thermal conditions.

2.1.1 Physical exchanger

Figure 3 (a) shows a picture of a small-scale FBR, consisting of 26 number of aluminum plates (Al-3003) in a parallel configuration. A summary of the geometrical details and thermophysical properties of the exchanger is provided in Table 1.

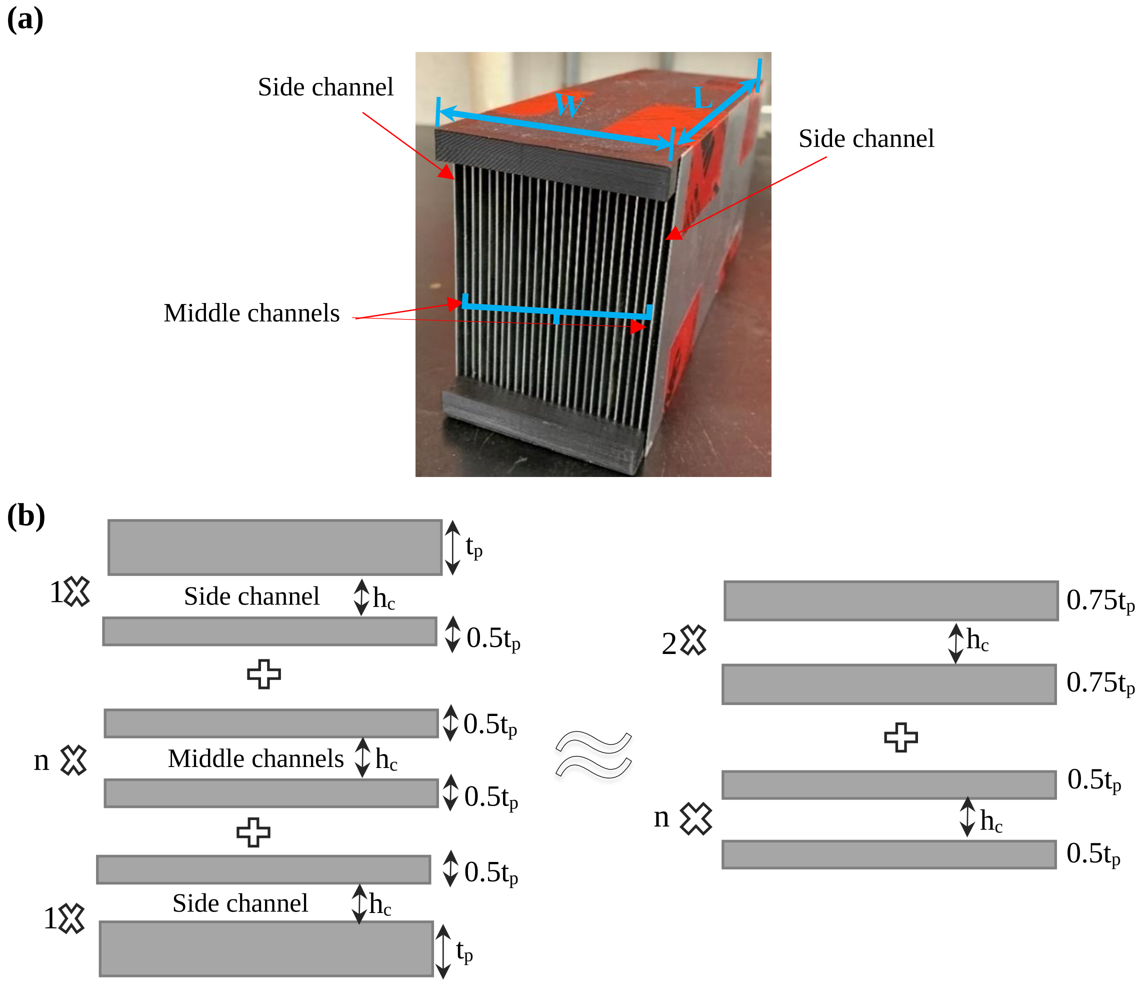

Figure 3: (a) Picture of the small-scale FBR, and (b) the proposed geometrical configuration for numerical modeling

Table 1. Geometrical details and thermophysical properties of the exchanger.

Air Channel	Length (L), (mm)	Width (W) (mm)	Hydraulic diameter (D_h) (mm)	Channel height (h_c) (mm)	Aspect ratio (α^*)
	200	80	4.08	2.1	0.03
Aluminum Plate	Thermal conductivity (k_m)(W/m·k)	Density (ρ_m) (kg/m^3)	Specific heat (Cp_m) (J/kg·K)	Thickness (t_p) (mm)	number of plates
	220	2730	904	0.7	26
Air properties	Thermal conductivity (k_g) (W/m·k)	Density (ρ_g) (kg/m^3)	Specific heat (Cp_g)(J/kg·K)	-	-
	0.024	1.23	1005	-	-

A representative parallel plate channel can be selected to perform numerical modeling. However, the side channels' boundary conditions (channels at both sides) are different from those in the middle. As shown in Fig. 3(a), the middle channels share their thickness (t_p) with the neighboring channels, while the side channels share only one plate thickness (tp) with the neighboring channels. Therefore the middle and side channels should be treated differently. Figure 3(b) illustrates the proposed channel configuration of the exchanger for numerical modeling purposes. As shown in Fig. 3(b), it is assumed that the exchanger comprises 'n' middle channels with a thickness of $0.5t_p$ and two channels with a thickness of $0.75t_p$. The weighted average outlet temperature of the middle and side channels is considered to be the outlet temperature of airstreams at the outlet of FBR.

2.1.2 Assumptions

The assumptions used in the model of the FBR are listed below:

i. The heat transfer process is modeled using the bulk air temperature; hence the numerical modeling of FBR is simplified to one-dimensional for the airflow.
ii. The temperature gradient across the thickness and the width of the matrix are considered to be negligible [26] ($Bi<0.1$), and the matrix temperature is assumed to vary only in the longitudinal direction.
iii. The velocity and temperature profiles of air streams develop simultaneously inside the channel [26] ($Pr=0.7$).
iv. The thermophysical properties of the air and matrix are constant.
v. Frosting and condensation do not happen in the exchanger.
vi. The switching between hot and cold airflows happens instantaneously.

Condensation and frosting are practical problems that might limit the application of FBRs in HVAC applications. Often energy exchangers are selected and operated to avoid any condensation or frosting within FBRs. Nizovtsev et al. [18] studied the impact of condensation on regenerative heat exchangers.

2.1.3 Governing equations

A schematic diagram of the representative channel and the heat transfer process between the hot and cold airstreams and the matrix are presented in Fig.4. The flow configuration is counterflow, and the one-dimensional governing energy equations for the airstream (subscript 'g') and matrix (subscript 'm'), considering the above-mentioned simplifying assumptions, are presented in Eqns. (1) and (2) [27,28]:

$$\rho_g Cp_g A_g \frac{\partial T_g}{\partial t} + V\rho_g Cp_g A_g \frac{\partial T_g}{\partial x} + h\frac{A_s}{L}\left(T_g - T_m\right) = \frac{\partial}{\partial x}\left(k_g A_g \frac{\partial T_g}{\partial x}\right) \quad (1)$$

$$\rho_m C_{P_m} A_m \frac{\partial T_m}{\partial t} - h\frac{A_s}{L}\left(T_g - T_m\right) - \frac{\partial}{\partial x}\left(k_m A_m \frac{\partial T_m}{\partial x}\right) = 0 \quad (2)$$

where T, x, ρ, C_p, k, V, h, L, and t are temperature, axial coordinate, density, specific heat capacity, thermal conductivity, mean airflow velocity, convective heat transfer coefficient, length of channel and time respectively. Other symbols, as used in the above equations (1 &2), are the cross-sectional area of the channel (A_g), matrix (A_m), and heat transfer surface area (A_s).

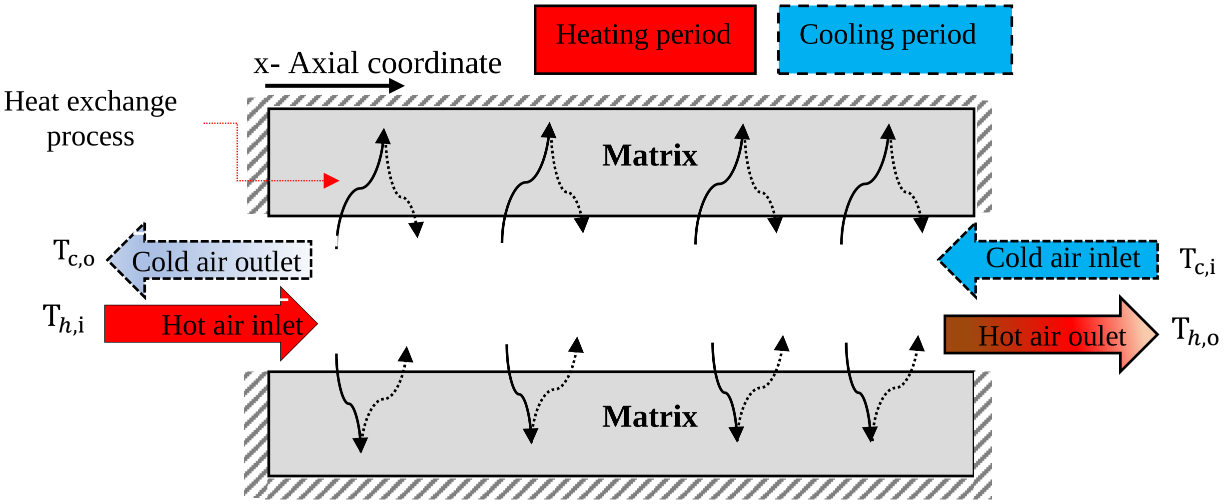

Figure 4: Schematic showing the heat transfer process in the representative channel of FBR

2.1.4 Boundary conditions

The inlet conditions of hot and cold airstreams are presented in Eqns. (3) and (4).

$$T_g(x = 0, mP \le t \le mP + P_h) = T_{h,i} \quad (3)$$

$$T_g(x = L, mP + P_h \le t \le (m + 1)P) = T_{c,i} \quad (4)$$

where $T_{h,i}$ and $T_{c,i}$ are the inlet temperature of the hot and cold airstreams, respectively. P is the total cycle time, P_h is the heating period, P_c is the cooling period and m is an integer to count the cycles of operations.

The ends of the matrix are assumed to be adiabatic [27,28]:

$$\left.\frac{\partial \mathrm{T_m}}{\partial \mathrm{x}}\right|_{\mathrm{x}=0} = \left.\frac{\partial \mathrm{T_m}}{\partial \mathrm{x}}\right|_{\mathrm{x}=\mathrm{L}} = 0 \quad (5)$$

2.1.5 Convective heat transfer coefficient

For laminar flow inside a channel with Reynolds number between 100-800, the hydrodynamic and thermal entry region is about 5-30% of the total length of the channel [29]. The airflow in FBR is laminar and within this range of Reynolds number; thus, the convective heat transfer coefficient for the simultaneous (thermal and hydrodynamic) developing flow should be used for the modeling [30].

The small-scale FBR exchanger (Fig. 2) is a rectangular channel with an aspect ratio (α^*) of 0.03. Although the developing Nusselt number (as a function of dimensionless axial distance $x^*(x/D_h \cdot Re \cdot Pr)$) are available for rectangular channels with several aspect ratios in literature [30], the developing Nusselt number is not available for the aspect ratio of the rectangular channel in this study ($\alpha^*=0.03$). Thus, the developing Nusselt number is approximated using Eqn. (6).

$$\mathrm{Nu}\ (\alpha^*) = \mathrm{Nu_{FD}}(\alpha^* = 0) \cdot \mathrm{Nu}^* \cdot \mathrm{Nu}_2^*(\alpha^*) \quad (6)$$

Where $\mathrm{Nu}\ (\alpha^*)$ is the developing Nusselt number for a rectangular channel with an aspect ratio of α^*. ($\mathrm{Nu}^* = \mathrm{Nu}_{(\alpha^*=0)}/\mathrm{Nu}_{(\mathrm{FD},\ \alpha^*=0)}$) is normalized developing Nusselt number for the parallel plate channel $(\alpha^* = 0)$ and $\mathrm{Nu}_2^*(\alpha^*) = \mathrm{Nu}_{\mathrm{FD},\alpha^*}/\mathrm{Nu}_{(\mathrm{FD},\alpha^*=0)}$ is normalized fully developed Nusselt number. Fully developed Nusselt number ($\mathrm{Nu}_{\mathrm{FD},\alpha^*}$) for rectangular channels as a function of aspect ratio (α^*) is presented in Eqn. (7) [30]:

$$\mathrm{Nu_{FD}} = 8.235\left[1 - 2.0421\alpha^* + 3.0853\alpha^{*2} - 2.4765\alpha^{*3} + 1.0578\alpha^{*4} - 0.1861\alpha^{*5}\right] \quad (7)$$

Figure 5 (a) shows $Nu^*(\alpha^* = 0)$, and Fig. 5 (b) represents Nu_2^* versus the rectangular aspect ratio.

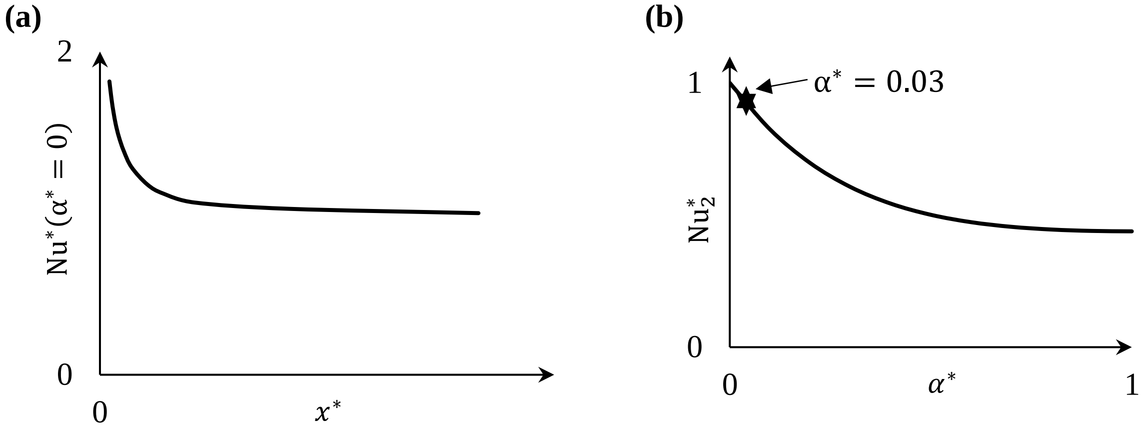

Figure 5: (a) Normalized developing Nusselt number for parallel plate ($\alpha^* = 0$) and normalized fully developed Nusselt number of rectangular channel versus α^*

2.1.6 Performance criteria

The performance of an FBR is quantified using the sensible effectiveness, which is defined as the ratio of the actual heat transfer rate to the maximum possible heat transfer rate [31,32], and is mathematically represented as follows:

$$\varepsilon = \frac{(\dot{\mathrm{m}}C_p)_h\left(\overline{\mathrm{T}}_{\mathrm{h,o}} - \mathrm{T}_{\mathrm{h,i}}\right) or (\dot{\mathrm{m}}C_p)_c\left(\overline{\mathrm{T}}_{\mathrm{c,o}} - \mathrm{T}_{\mathrm{c,i}}\right)}{\min\left((\dot{\mathrm{m}}C_p)_h, (\dot{\mathrm{m}}C_p)_c\right)\ \left(\mathrm{T}_{\mathrm{h,i}} - \mathrm{T}_{\mathrm{c,i}}\right)} \tag{8}$$

where $\mathrm{T}_{\mathrm{h,i}}, \mathrm{T}_{\mathrm{c,i}}$ are the inlet temperature of the hot and cold airflows respectively, while $(\dot{\mathrm{m}}C_p)_h$ and $(\dot{\mathrm{m}}C_p)_c$ are the hot and cold stream heat capacity rate, respectively. As noted previously, the temperature of the air leaving an FBR varies with time, and $\overline{\mathrm{T}}_{\mathrm{h,o}}$, $\overline{\mathrm{T}}_{\mathrm{c,o}}$ are the time-averaged outlet temperatures of hot and cold airstreams, respectively, and are mathematically represented by Eqns. (9) and (10).

$$\overline{\mathrm{T}}_{\mathrm{h,o}} = \frac{1}{P_h}\int_0^{P_h} T_{h,o}\,dt \tag{9}$$

$$\overline{\mathrm{T}}_{\mathrm{c,o}} = \frac{1}{P_c}\int_0^{P_c} T_{c,o}\,dt \tag{10}$$

2.2 Temperature sensor model

2.2.1 Physical model and assumptions

The temperature sensors at the outlet of FBRs are immersed in the airstreams, whose temperature varies with time within each period. It is assumed that the resistance to the heat conduction of the temperature sensor is much smaller than the resistance to convection across the airstream. This is a reasonable assumption as the temperature sensors are usually made small. Thus, the temperature of the sensor is uniform at any time, and the lumped capacitance method is applicable and valid [26]. Another assumption is that sensors thermal properties are constant, and the exchange of radiation heat exchange with the surrounding environment is insignificant.

2.2.2 Governing equation

With the assumption of the validity of the lumped capacitance method [26], the energy equation for temperature sensors is given in Eqn. (11).

$$\left(\mathrm{T_g} - \mathrm{T_s}\right) = \frac{\rho_{\mathrm{ts}} \mathrm{V_{ts}} \mathrm{Cp_{ts}}}{\mathrm{hA_{ts}}} \frac{\mathrm{dT_s}}{\mathrm{dt}} = \tau_{\mathrm{s}} \frac{\mathrm{dT_s}}{\mathrm{dt}} \tag{11}$$

where ρ_{ts}, $\mathrm{V_{ts}}$, $\mathrm{Cp_{ts}}$, $\mathrm{A_{ts}}$ are the density, volume, specific heat capacity, and surface area of the temperature sensor, respectively. h is the convective heat transfer coefficient, and $\mathrm{T_s}$ is the temperature of the sensor (sensor measurement), while $\mathrm{T_g}$ is the air temperature. τ_{s} ($= \frac{\rho_{\mathrm{ts}} \mathrm{V_{ts}} \mathrm{Cp_{ts}}}{\mathrm{hA_{ts}}}$) is the time constant of the sensor, which is defined as the time it takes to reach 63.2% of the total difference between the initial and final temperature [26].

2.2.3 Sensor initial condition

Before exposure to the airflow at the outlet of the exchanger (FBR), the initial sensor temperature is presented in Eqn. (12).

$$\mathrm{T_{s,0}} = \mathrm{T_{initial}} \tag{12}$$

2.3 Combined FBR and sensor model

FBR model predicts the actual temperature of the air at the outlet of FBR. With the temperature ($\mathrm{T_g}$) from the FBR model, the sensor temperature measurement is obtained using the sensor model in Eqn. (11). The combined FBR and sensor model take the actual temperature from the FBR model and use this to obtain the sensor measurements from Eqn. (11). The time constants for the sensors can be obtained experimentally or from the manufacturer's datasheet.

2.4 Numerical solution for the FBR model

The transient transport equations for the conservation of energy in airflow and matrix (Eqns. (1) and (2)) are discretized using the finite volume method [33]. The upwind differencing and the central differencing schemes are used to approximate the convection term for the airflow and the diffusion term in the matrix. The resulting algebraic equations for the airflow are solved using the Gauss-Seidel iteration technique, while the Tridiagonal Matrix Algorithm is used to solve the energy equation in the matrix.

The numerical solution starts with initial values for the air and matrix temperatures. Although the quasi-steady-state condition is used for the performance calculation of FBR, the current numerical solution is time accurate, and time is incremented whenever the following convergence criterion (Eqn. (13)) is satisfied for the dependent variables; i.e., the air and matrix temperatures:

$$\frac{\sum_{\mathrm{i=1}}^{\mathrm{N_s}}\left(\mathrm{T(i)^{j+1}-T(i)^{j}}\right)}{\mathrm{N_s}\times\left(\mathrm{T_{h,i}-T_{c,i}}\right)}\le 10^{-5} \tag{13}$$

where T is the temperature (air and matrix), N_s is the numbers of spatial nodes, and i, j are integers. The convergence criterion is selected to be 10^{-5} as decreasing this value to 10^{-6} has a negligible effect (less than 0.05%) on the predicted effectiveness.

The outlet temperature of airstreams in FBRs varies with time, but exchanger reaches a quasi-steady-state condition. At this condition, the outlet temperature of FBR varies with time but repeats itself in a cyclic version [14]. The onset operating condition of a quasi-steady state is identified using Eqns. (14) and (15) [34].

$$\left|\frac{\dot{\mathrm{m}}_{\mathrm{h}}\left(\mathrm{T_{h,i}-T_{h,o}}\right)-\dot{\mathrm{m}}_{\mathrm{c}}\left(\mathrm{T_{c,o}-T_{c,i}}\right)}{\min(\dot{\mathrm{m}}_{\mathrm{h}},\dot{\mathrm{m}}_{\mathrm{c}})\left(\mathrm{T_{h,i}-T_{c,i}}\right)}\right|\le 10^{-2} \tag{14}$$

$$\left|\frac{\partial\epsilon}{\partial \mathrm{t}}\right|\approx\left|\frac{\epsilon^{\mathrm{k}}-\epsilon^{\mathrm{k-1}}}{\mathrm{P}}\right|\le 10^{-4} \tag{15}$$

where ϵ is the effectiveness of FBR, and $\dot{m}_h$, $\dot{m}_c$ are the hot and cold mass flowrate respectively. ϵ^k and ϵ^{k-1} are the effectiveness at the current and previous cycles, respectively. Decreasing the quasi-steady-state conditions criteria (10^{-2} and 10^{-4}) in Eqns. (14) and (15) by a factor of 10 has an insignificant effect (less than 0.1%) on the predicted quasi-steady-state effectiveness, whereas increasing the solution time by approximately a factor of two. A Matlab code has been developed to solve the algebraic equations. A flowchart presented in Fig. 6 shows the numerical procedure to solve the FBR and sensor model's governing equations.

The numerical solution is carried out within a uniform spatial grid with a constant time step. The grid independence test is performed to determine the grid size and time step for the numerical solution. It is observed that decreasing the spatial grid size to less than 0.0007m and time step less than 0.01s have a negligible effect (<0.1%) on the predicted effectiveness. Therefore, a time step of 0.01 s and a spatial grid size of 0.0007 m are selected for the numerical study.

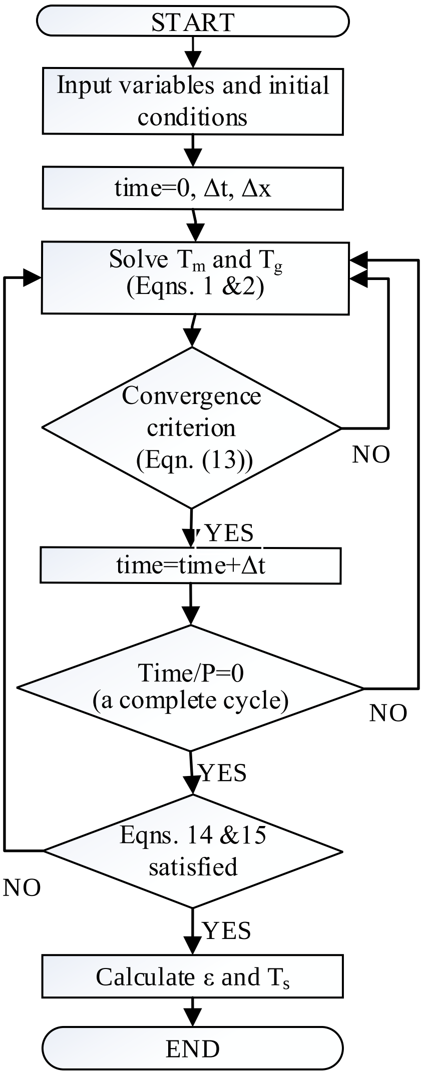

Figure 6: Numerical flowchart to solve the numerical problem

2.5 FBR model validation

The effectiveness-Number of Transfer Units (ε-NTU) method is a commonly used approach for the design of heat exchangers. Effectiveness can be presented as a function of dimensionless groups and flow arrangements [22]. The dimensionless groups are extracted from the governing equations, and for sensible regenerators, effectiveness can be obtained from Eqn. (16) and its functional terms are listed in Eqns. (17)-(20).

$$\epsilon = \phi(\mathrm{NTU}_0, C^*, C_r^*, (hA_s)^*) \tag{16}$$

where:

$$\mathrm{NTU_0} = \frac{1}{(\dot{m}C_p)_{g,min}}\left[\frac{1}{(hA_h)_h} + \frac{1}{(hA_c)_c}\right]^{-1} \tag{17}$$

$$\mathrm{Cr^*} = \frac{(MC_p)_m}{(\dot{m}C_p)_{g,min}(P_c + P_h)} \tag{18}$$

$$\mathrm{C^*} = \frac{(\dot{m}C_p)_{g,min}}{(\dot{m}C_p)_{g,max}} \tag{19}$$

$$(hA_s)^* = \frac{(hA_s)_h}{(hA_s)_c} \tag{20}$$

where $\mathrm{NTU_o}$, Cr*, C*, and $(hA_s)^*$ are the overall number of transfer units, overall matrix heat capacity ratio, the ratio of minimum to maximum heat capacity rate of the airstreams, and convective conductance ratio, respectively. For the range of $0.25 \leq (hA_s)^* \leq 4$, the effect of convective conductance ratio, $(hA_s)^*$on effectiveness is negligible [22].

Axial heat conduction in the matrix is significant in FBRs compared to rotary exchangers because of the higher thickness of plates, and it also decreases the effectiveness of regenerators [35,36]. Bahnke and Howard [35] proposed a dimensionless group (λ) (Eqn. (21)) to quantify the effect of axial conduction within the matrix:

$$\lambda = \frac{k_m A_{m,t}}{L\, C_{min}} \tag{21}$$

where k_m is the thermal conductivity and L is the length of the exchanger, $A_{m,t}$ $(= A_{m,h} + A_{m,c})$ is the total area for longitudinal conduction and C_{min} is the minimum heat capacity rate of the airflows. $A_{m,h}$ and $A_{m,c}$ are the matrix hot and cold side cross-sectional area, respectively.

Empirical correlations have been proposed for regenerators' sensible effectiveness as a function of dimensionless parameters [22,37]. Such correlations for different flow conditions are listed in sections 2.5.1 and 2.5.2.

2.5.1 Balanced flow condition

For the balanced flow regenerators ($C^* = 1$), effectiveness is obtained from Eqn. (23) [22]:

$$\epsilon = \frac{NTU_o}{1+NTU_o}\left[1-\frac{1}{9(Cr_o^*)^{1.93}}\right]\left[1-\frac{C_\lambda}{2-C^*}\right] \tag{23}$$

where:

$$C_\lambda = \frac{1}{1+\frac{NTU_0(1+\lambda\Phi)}{1+\lambda NTU_0}} - \frac{1}{1+NTU_0} \tag{24}$$

$$\Phi = \left(\frac{\lambda NTU_0}{1+\lambda NTU_0}\right)\tanh\left(\frac{NTU_0}{(\lambda NTU_0/1+\lambda NTU_0\ )^{0.5}}\right) \tag{25}$$

Eqn. (23) is accurate within 1% for the range of $1 \le NTU_o \le 20$, $2 \le Cr^* \le \infty$, $0.5 \le (\mathrm{hA})^* \le 1$ and $0 \le \lambda \le 0.08$.

2.5.2 Unbalanced flow condition

It is essential to evaluate the effect of unbalanced flow conditions on the predicted effectiveness since it frequently occurs in HVAC applications [34]. Therefore, the present study also entails the validation of the FBR model under unbalanced flow conditions. The effectiveness of such flow conditions can be obtained from Eqn. (26) as listed in the literature [22].

$$\epsilon = \frac{1-\exp\{\epsilon_{\mathrm{r},\lambda\neq0}(\mathrm{C}^{*2}-1)/[2\mathrm{C}^*(1-\epsilon_{\mathrm{r},\lambda\neq0})]\}}{1-\mathrm{C}^*\exp\{\epsilon_{\mathrm{r},\lambda\neq0}(\mathrm{C}^{*2}-1)/[2\mathrm{C}^*(1-\epsilon_{\mathrm{r},\lambda\neq0})]\}} \tag{26}$$

where:

$$\epsilon_{\mathrm{r},\lambda=0} = \frac{\mathrm{NTU}_{\mathrm{o,m}}}{1+\mathrm{NTU}_{\mathrm{o,m}}}\left[1-\frac{1}{9\left(\mathrm{Cr}_{\mathrm{o,m}}^*\right)^{1.93}}\right] \tag{27}$$

$$\epsilon_{\mathrm{r},\lambda\neq0} = \mathrm{C}_\lambda\epsilon_{\mathrm{r},\lambda=0} \tag{28}$$

$$\mathrm{NTU}_{\mathrm{o,m}} = \frac{2\mathrm{NTU}_0.\mathrm{C}^*}{1+\mathrm{C}^*} \tag{29}$$

$$\mathrm{Cr}_{\mathrm{m}}^* = \frac{2\mathrm{Cr}^*.\mathrm{C}^*}{1+\mathrm{C}^*} \tag{30}$$

In Eqn. (27), C_λ is obtained from Eqn. (24) using the values of $NTU_{o,m}$ and Cr_m^* computed from equations (29) & (30), respectively. The accuracy of Eqn. (26) is the same as Eqn. (23) presented in the previous subsection for the balance flow condition.

2.5.3 Validation of FBR model

Eqns. (23) and (26) are valid when $0 \leq \lambda \leq 0.08$, therefore the results of this present numerical (FBR model) model for FBRs are validated with the numerical results of Bahnke and Howard [35] whenever the operating condition is outside this range. Bahnke and Howard [35] results are valid for the range of dimensionless parameters:$1 \leq NTU_o \leq 100, 0.9 \leq C^* \leq 1, 1 \leq C_r^* \leq \infty,\ 0.01 \leq \lambda \leq 0.32,\ and\ 0.25 \leq (hA)^* \leq 1$.

The maximum effectiveness difference between the current FBR model results and results obtained from Eqns. (23) and (26) over the range of $1 \leq NTU_o \leq 20,\ 2 \leq Cr^* \leq 10$, $0.5 \leq (\mathrm{hA})^* \leq 1$ and $0 \leq \lambda \leq 0.08$ are found to be less than 1%. Furthermore, for higher values of conduction parameters ($0.08 \leq \lambda \leq 0.32$), the predicted effectiveness from the FBR model is in agreement with the numerical results of Bahnke and Howard [35] with a maximum difference of 0.5%. Figure 7 presents an example of comparisons between the current FBR model and the relevant literature [22,35] results for balanced/unbalanced flow FBRs.

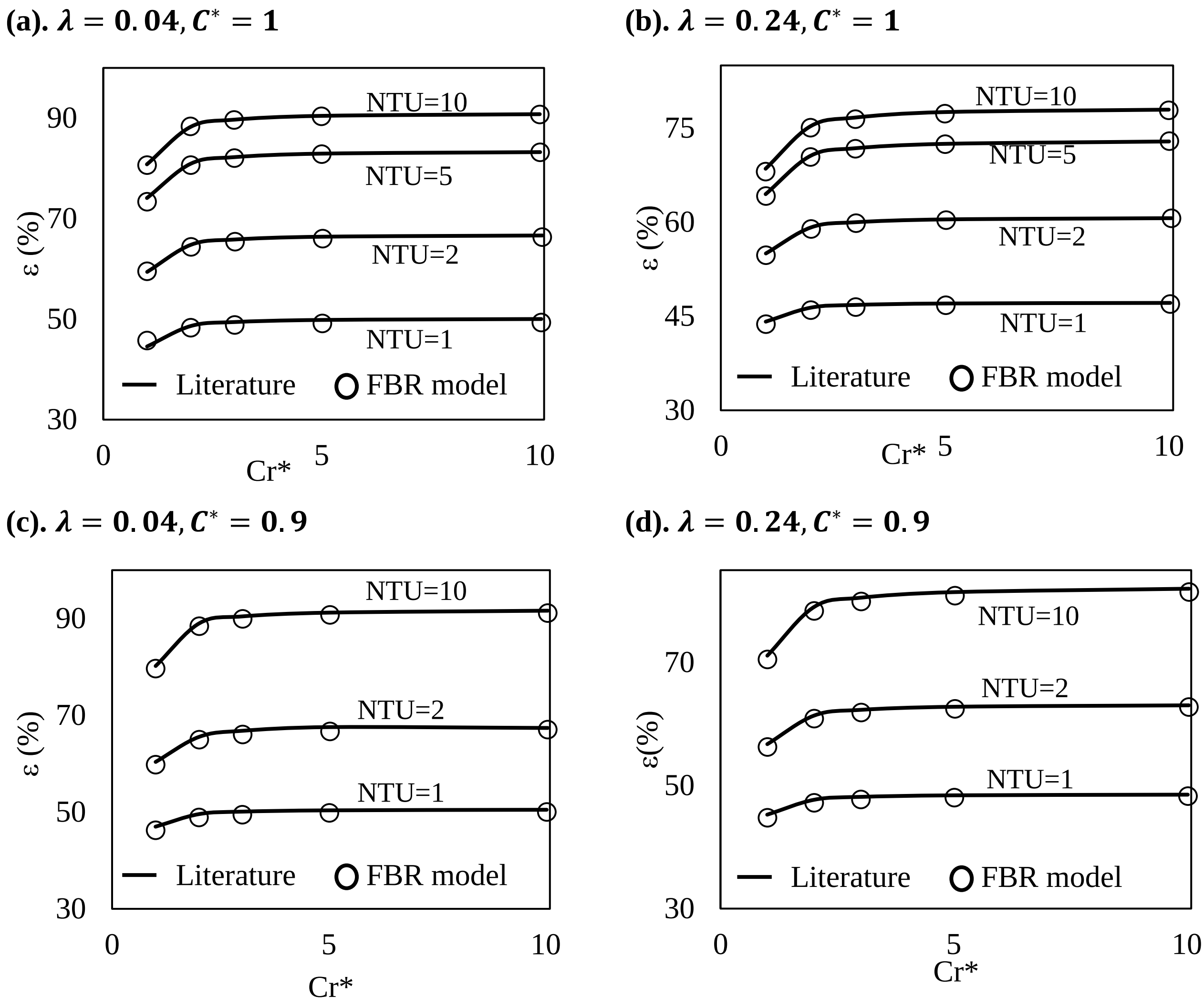
(a). $\boldsymbol{\lambda = 0.04, C^* = 1}$

(b). $\boldsymbol{\lambda = 0.24, C^* = 1}$

(c). $\boldsymbol{\lambda = 0.04, C^* = 0.9}$

(d). $\boldsymbol{\lambda = 0.24, C^* = 0.9}$

Figure 7: Comparison of results of the FBR model and the literature [22,35] for balanced and unbalanced flow conditions ($\lambda = 0.04, 0.24$).

2.6 Validation of the combined FRB and sensor model

The combined FBR and sensor model results are validated with the results from a small-scale test facility, as the experimental data includes both FBR and the sensor effects. The combined model validation includes validation of (1) transient temperature profile before reaching the quasi-steady state, (2) transient during the quasi-steady state, and (3) sensible effectiveness with experimental results from the small-scale test facility.

2.6.1 Small-scale experimental facility

The small-scale test facility is developed to determine the effectiveness of FBRs. The test facility consists of supply lines (hot and cold airstreams) and a test section. The supply airlines provide continuous conditioned air to the test section. A schematic of the test section is shown in Fig. 8. The thick insulation inside the test section substantially reduces the heat transfer between the exchanger and its surroundings. A pneumatic-powered linear actuator unit is used to slide the exchanger cyclically between the hot and cold airstreams within the test section. The exchanger in the test section is alternatively exposed to the hot and cold airstreams to simulate the alternate heating and cooling processes of FBRs. The exchanger movement time between airflow is fast, and it takes 0.3s to slide the exchanger between the air streams. Temperature is measured using T-type (0.08 mm wire diameter) thermocouples. The uncertainty in temperature measurements is ±0.2°C, and constant temperature at the exchanger inlet is maintained with a maximum temperature deviation of ±0.3°C. A detailed description of the facility development, measurement procedures, and uncertainty analysis can be found in the previous work of the authors of this paper [20].

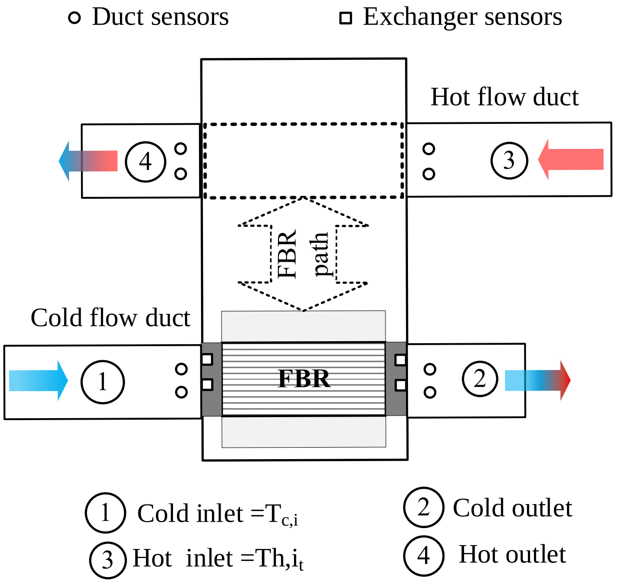

Figure 8: Schematic of the test section and thermocouples to measure the air temperature

To measure the air temperature at the outlet of the exchanger, a set of temperature sensors (thermocouples) are attached to the exchangers (called exchanger sensors), and another set is fixed to the airflow ducts (called duct sensors), as shown in Fig.8. The duct sensors do not move with the exchanger, while the exchanger sensors are moved between airstreams along with the exchanger. The initial temperatures of the duct and exchanger sensors are different because of their exposure to different airstreams during the previous period. For the heating and cooling periods, the initial temperatures of the duct and exchanger sensors are as follows.

For the duct sensors:

$$\mathrm{T_{initial} = T_{h,i}} \quad \text{for heating period} \tag{31}$$

$$\mathrm{T_{initial} = T_{c,i}} \quad \text{for cooling period} \tag{32}$$

For the exchanger sensors:

$$\mathrm{T_{initial} = T_{c,i}} \quad \text{for heating period} \tag{33}$$

$$\mathrm{T_{initial} = T_{h,i}} \quad \text{for cooling period} \tag{34}$$

Table 2 provides the operating conditions of the experiments used for the validation of the combined FRB and sensor model. The time constant of the thermocouples used in the test facility is obtained experimentally.

Table 2. Operating conditions and sensor time constant for the validation of results

Flow rate		Inlet temperature (°C)		face velocity	Cycle time	Re	NTU$_o$	Cr*	Sensor time constant (s)
(L/s)	(kg/s)	Hot side	Cold side	(m/s)	(s)				
7.6	0.00926	40.0	24.0	2.0	20-240	520	2.4	0.8-10	1.5

2.6.2 Transient temperature before quasi-steady-state

The FBR outlet temperature measurements from the exchanger sensors, and the combined FBR and sensor model, are presented in Fig. 9. Before the start of the experiment, the exchanger matrix is at the cold flow temperature ($T_{c,i}$). At time zero, the exchanger is moved to the hot flow duct, and hot air flows through the exchanger and heats the exchanger matrix (for 60 s). The exchanger is then moved to the cold flow duct and cools the airflow (for 60 s). This alternate movement of the exchanger between the airflows is continued until the exchanger's outlet temperature reaches the quasi-steady-state condition. Figure 9 shows that the combined FBR and sensor model temperatures are in good agreement with the experimental measurements during the entire transient process before reaching the quasi-steady state condition. It is important to note that the exchanger sensor's initial conditions at the beginning of heating and cooling periods are the cold inlet flow and hot inlet flow temperatures, respectively, as presented in Eqns. (33) and (34). Also, the combined FBR and sensor model and the experimental results agree well at the beginning of heating and cooling periods, where the sensor effect appears to be significant.

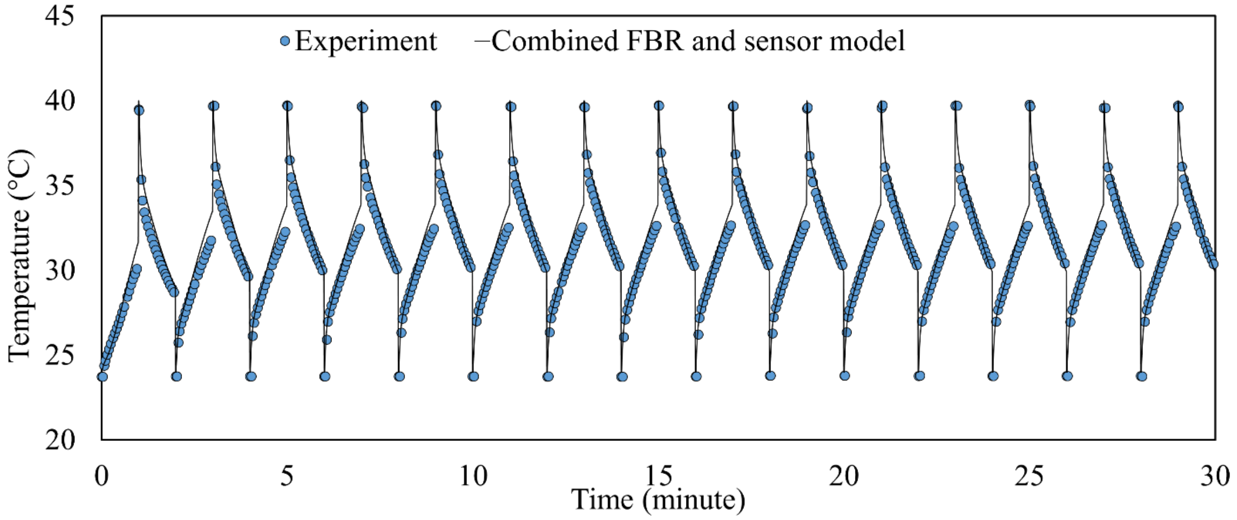

Figure 9: Transient outlet temperature profile of FBR, a comparison between combined FBR and sensor model and experimental results from exchanger sensors (NTU=2.4, face velocity=2.0 m/s, sensor time constant =1.5 s)

2.6.3 Quasi-steady-state temperature validation

A comparison between the experimental and numerical results (both the FBR model and the combined FBR and sensor model) for temperature profile at the quasi-steady-state condition is presented in this section. Figure 10 shows the experiment's temperature profiles with the duct sensors, FBR model, and combined FBR and sensor model, along with the inlet temperatures. A schematic of the FBR test facility is included in this figure to enhance the demonstration and understanding of the temperature profiles. The experimental and the FBR model temperatures are in good agreement, except at the beginning of heating and cooling periods, as shown in Fig.10. The observed difference can be attributed to the transient response of the temperature sensors. The initial temperatures of the duct sensors in the heating/cooling period are equal to the inlet hot/cold temperatures (Eqns. (31) and (32)). It takes some time for the duct sensors to respond to the change in temperature during heating and cooling periods. The combined FBR and sensor model captures this initial transient behavior, and the combined model results are in good agreement with the experimental measurement for the entire heating and cooling periods.

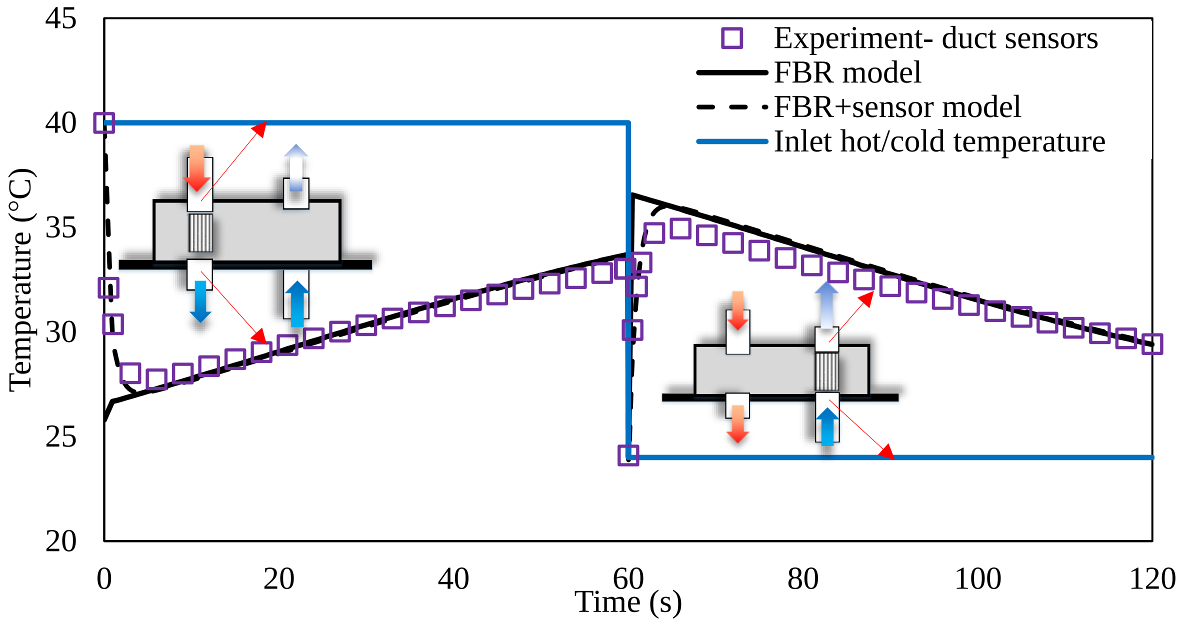

Figure 10: Quasi-steady-state temperature profile from the experiment with duct sensors, FBR model, and combined FBR and sensor model as well as the inlet temperatures (NTU=2.4, face velocity=2.0 m/s, sensor time constant =1.5 s)

Figure 11 presents the same temperature profiles as in Fig. 10; however, the experimental measurements are shown for the exchanger sensors. Again, the temperature profile from the experiment and the numerical model of the FBR model are in good agreement except at the beginning of heating and cooling periods due to the transient response of temperature sensors. For the heating period, the exchanger sensors' initial temperature is equal to the cold inlet temperature (Eqn. (33)). Similarly, the exchanger sensors are initially at the hot inlet temperature during the cooling period (Eqn. (34)). With the combined FBR and sensor model, this initial transient behavior of sensors is included in the model, and the comparison between this combined model and experimental temperature profiles exhibits a good agreement, as seen in Fig. 11.

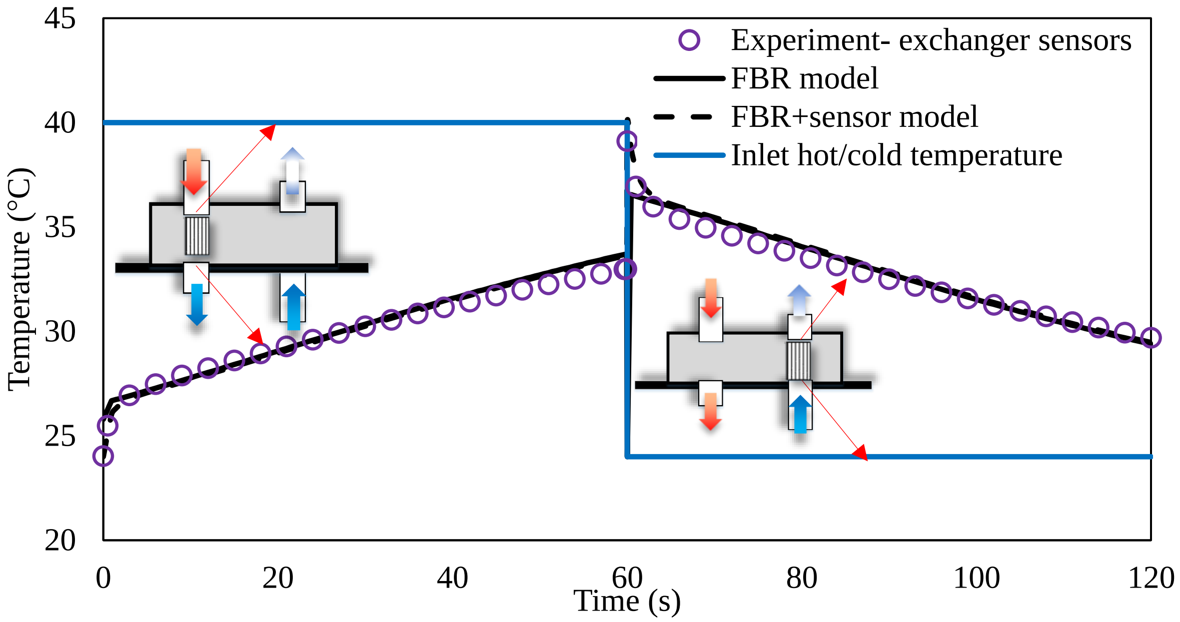

Figure 11: Quasi-steady-state temperature profile from the experiment with exchanger sensors, FBR model, and combined FBR and sensor model as well as the inlet temperatures (NTU=2.4, face velocity=2.0 m/s, sensor time constant =1.5 s)

Figure 12 shows the comparison of the quasi-steady-state temperature profile (from the FBR model), and the experimental results (from both the duct and exchanger sensors). The measurements from the duct and exchanger sensors are different at the beginning of heating/cooling periods, but after about six seconds in each period, both duct and exchanger sensor temperature measurements become almost equal, as seen in Fig.12. The sensor measurements after the initial trainset region are also in good agreement with the FBR model. The good agreement between the FBR model and experimental measurements after this initial transient is further evidence of the significance of the sensor transient response to the temperature change in FBRs.

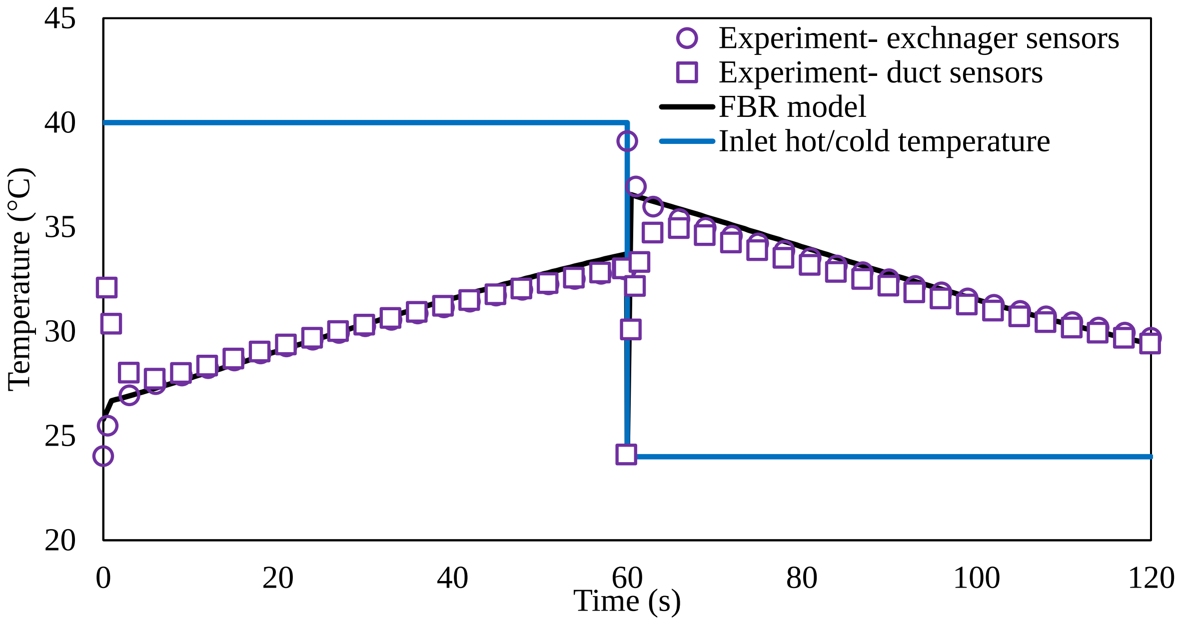

Figure 12: Quasi-steady-state temperature profile from the experiment with duct and exchanger sensors, FBR model, as well as the inlet temperatures (NTU=2.4, face velocity=2.0 m/s, sensor time constant =1.5 s)

Except at the beginning of each period, the air temperature varies linearly through the rest of the periods. Krishnan et al. [20,38] utilized this linear behavior to modify the temperature profile at the beginning of periods. The modification involves using a linear "backfit" method to modify the temperature profile to consider the initial trainset region resulting from temperature sensors' transient response.

3 Sensible effectiveness

The experimental results obtained in this study are modified according to the linear backfit method presented by Krishnan et al. [20], and the adjusted experimental effectiveness values are compared with the current FBR model results, and graphical representation is provided in Fig. 13. The numerical results agree with the modified experimental data within the range of experimental uncertainty.

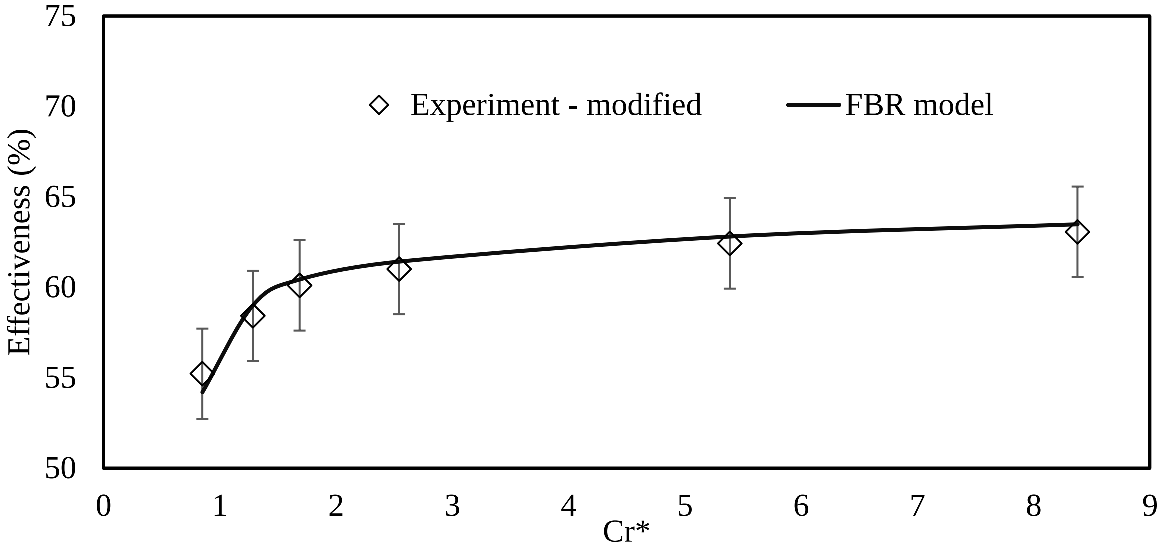

Figure 13: FBR effectiveness from the experiment and the FBR model (NTU=2.4, face velocity=2.0 m/s, sensor time constant =1.5 s)

3.1 Effect of non-instantaneous movement of exchanger between ducts on the predicted effectiveness

In the FBR model development, it is assumed that the exchanger movement between the two airflow ducts happens instantaneously. It takes time (around 0.3 s) for the exchanger to move between the airflows in an actual situation. To estimate the error due to this non-instantaneous movement of the exchanger between airflow ducts, the inlet velocity is assumed to change gradually (exponentially) during the exchanger movement. This velocity profile (corresponding to the non-instantaneous movement of the exchanger (V_{NS})), along with the assumed constant velocity profile (V) (corresponding to the rapid movement of exchanger between airflow ducts in the numerical modeling), are presented in Fig. 14.

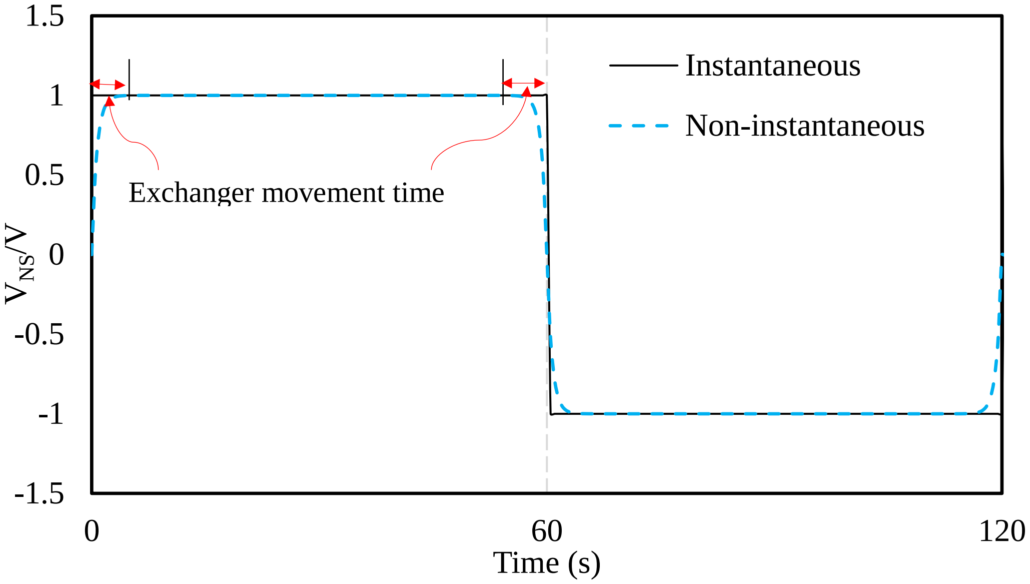

Figure 14: Velocity profiles corresponding to the instantaneous and non-instantaneous movement of exchanger between the airflow ducts

Figure 15 shows the changes in effectiveness that occur when the switching between airstreams is not instantaneous for the range of Cr^* between 0.8 and 9 (P_h=P_c=10-90 s). The results (Fig. 15) show that including the exchanger movement with a switching time of 1 second in the model increases the effectiveness by less than 0.4%, and with 0.3 seconds switching time, the maximum effectiveness change is less than 0.3%. Thus, the assumption of instantaneous movement of exchanger between the ducts is valid and does not have any significant effects on the predicted results from the FBR model.

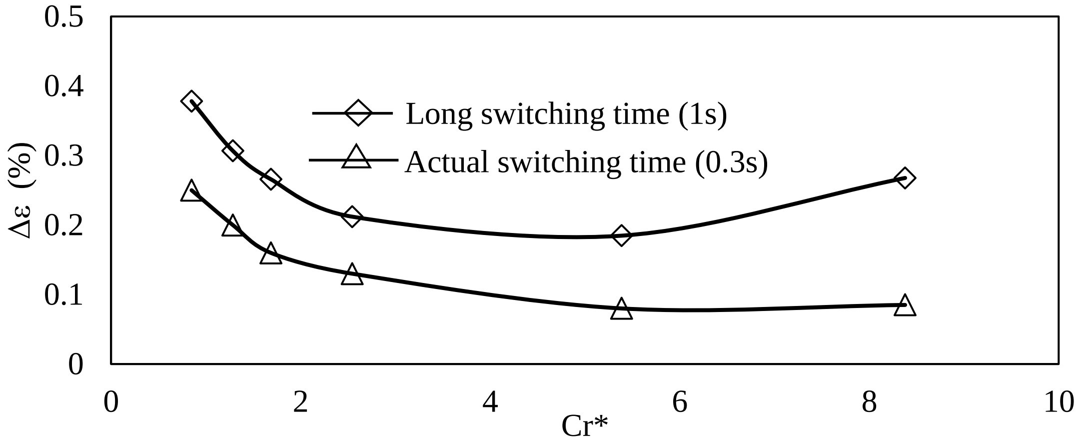

Figure 15: Changes in effectiveness when exchanger movement time is included in the model ($\Delta\varepsilon=\varepsilon_{movement} - \varepsilon_{instantaneous\ movement}$)

4 Applications of the combined FBR and sensor model

The developed model (combined FBR and sensor) is applied to evaluate the temperature profile and effectiveness of FBRs under the operating conditions suitable for HVAC applications. The performance under the operating conditions of balanced/unbalanced flow rate and equal/unequal heating and cooling period are compared. The FBR model's temperature is the actual air temperature; thus the difference between the FBR model's effectiveness and the combined FBR and sensor models is called "effectiveness error.", and mathematically represented by Eqn. (35).

$$\Delta\epsilon = \epsilon_{(FBR\ model)} - \epsilon_{(combined\ FBR\ and\ sensor\ model)} \tag{35}$$

Effectiveness error is the error due to the transient response of sensors. These errors are obtained for both the duct and exchanger sensors over the range of cycle time of 20-240 seconds and at the operating conditions presented in Table 2.

4.1 Quasi-steady-state temperature and effectiveness of a balanced FBR

Figure 16 represents the temperature profiles from the FBR model and the combined FBR and sensor models (with duct sensors) at two different cycle times (15 and 120 seconds) under a balanced flow rate condition for an FBR. The effect of the sensor response to the transient temperature of FBR for the shorter cycle duration is noticeably significant than the extended cycle time. As shown in Fig. 16 with dotted circles, the sensor temperature measurements at 15 s cycle time deviated from the actual temperature profile for almost 70% of heating/cooling period duration, while this deviation is only 10% for the 120 s cycle time.

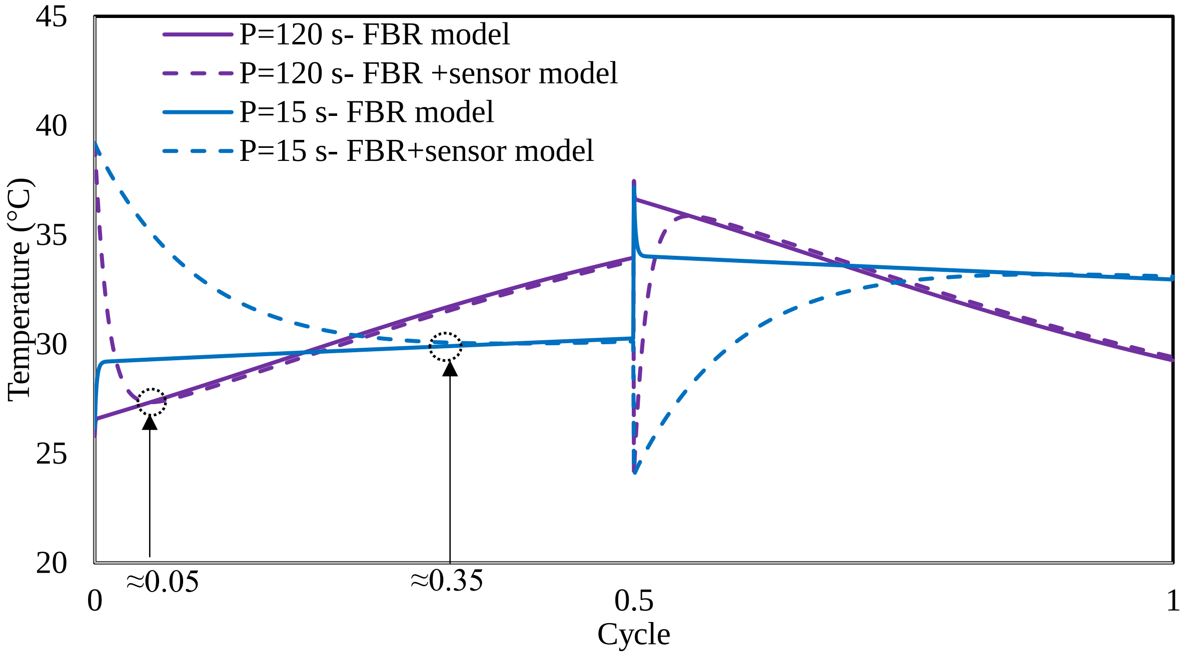

Figure 16: Comparison of temperature profiles from the FBR and combined FBR and sensor model (time constant=1.5 s) at P=120, 15 s (NTU=2.4, face velocity=2.0 m/s, time constant =1.5 s)

Figure 17 presents the effectiveness error due to sensors' response with a time constant of 1.5 s for both duct and exchanger sensors at different cycle times using Eqn. (35). The effectiveness error decreases for both sensors' locations (duct and exchanger) when cycle time increases. While sensors located at the duct underestimate the effectiveness, exchanger sensors overestimate the measured effectiveness values. Although the effectiveness error is small (less than 1%) at 240 seconds, these errors are significant for the 15 seconds cycles. The effectiveness errors (Fig. 17) are approximately 12% and 8% for the duct and exchanger sensors at cycle time 15 s, respectively.

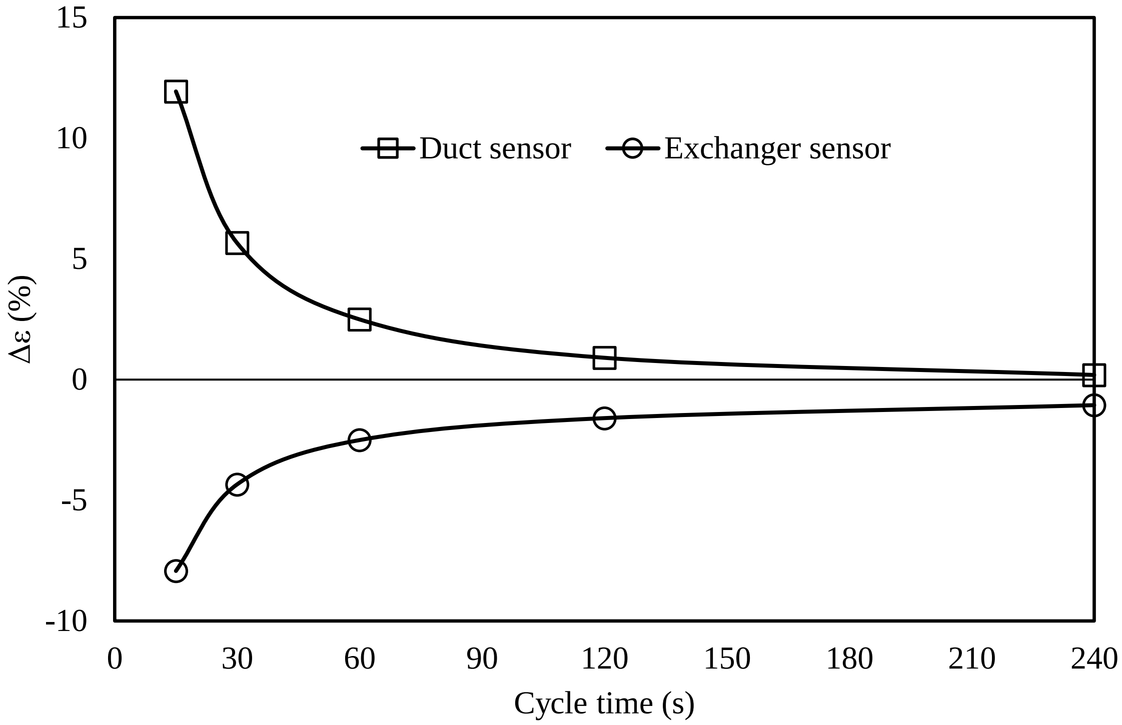

Figure 17: Effectiveness error (Δε) for the duct and exchanger sensors for a balanced flow rate (NTU=2.4, face velocity=2.0 m/s) at different cycle times (time constant=1.5 s)

4.2 Unbalanced flow rate

Figure 18 represents the temperature profile for an unbalanced flow ($C^* = \mathrm{C_{cold}}/\mathrm{C_{hot}}$ =0.9), and the temperature profile from the combined FBR and sensor model for the duct sensor with a time constant of 1.5 s. The balanced flow rate profile is also included for ease of comparison. The average temperatures of the unbalanced exchanger are higher in the hot and cold periods compared to those of the balanced exchanger.

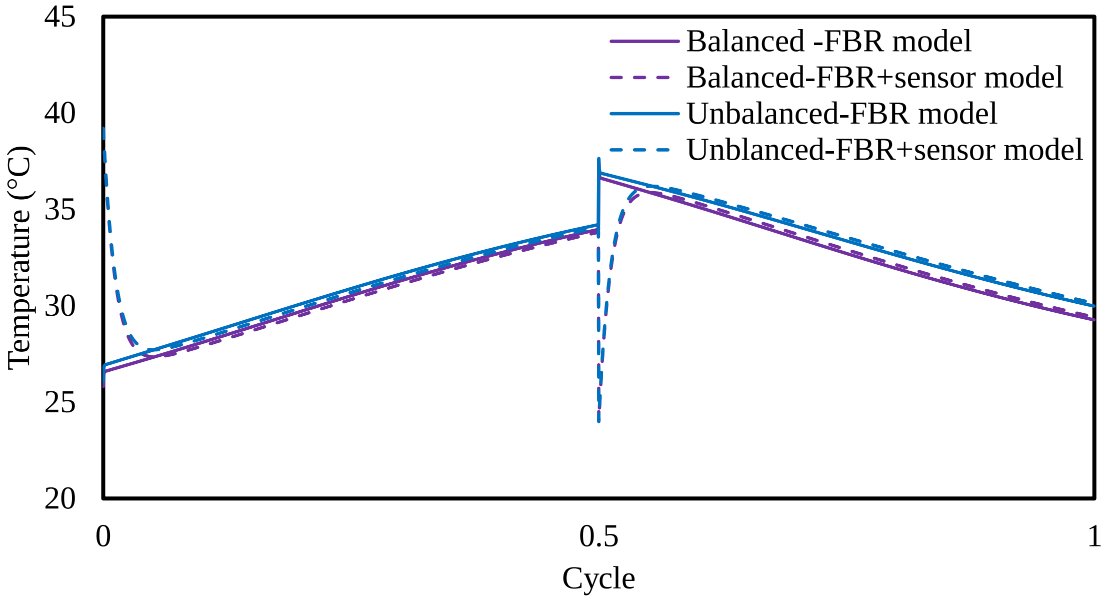

Figure 18: Comparison of temperature profiles from the FBR and combined FBR and sensor model for balanced and unbalanced flow exchanger at 120 s cycle duration (face velocity=2.0 m/s, time constant =1.5 s)

Figure 19 shows the comparison of the effectiveness error for balanced and unbalanced FBR at different cycle durations. Compared to the balanced FBR, the effect of sensor response is slightly larger in the unbalanced FBR. In the unbalanced flow condition, the exchanger sensor is more sensitive when compared to the duct sensors.

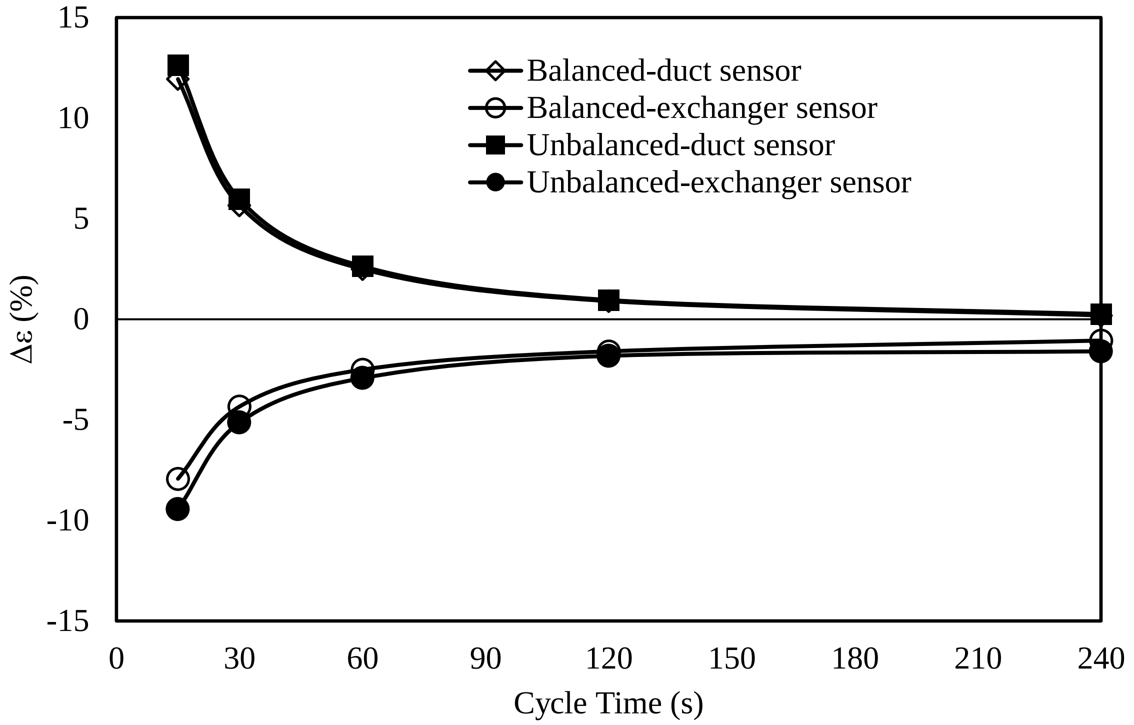

Figure 19: Effectiveness error (Δε) of balanced and unbalanced FBR from the duct and exchanger sensors at different cycle times (face velocity=2.0 m/s, time constant=1.5 s)

4.3 Heating and cooling periods (with balanced flow rate)

The duration of heating and cooling periods (P_h and P_c) could be unequal in the HVAC applications [1]. The temperature profile from the FBR model and the combined FBR and sensor model (for a duct sensor with a time constant of 1.5 seconds) are presented in Fig. 20, for equal ($P_h = P_c = 0.5\ P$) and unequal ($P_h = 0.25\ P\ , P_c = 0.75\ P$) heating/cooling periods. The flow rate is maintained balanced in this section. The cycle time is 120 seconds, and all other parameters are kept constant. The average period temperature for the unequal periods is lower than that of the equal periods.

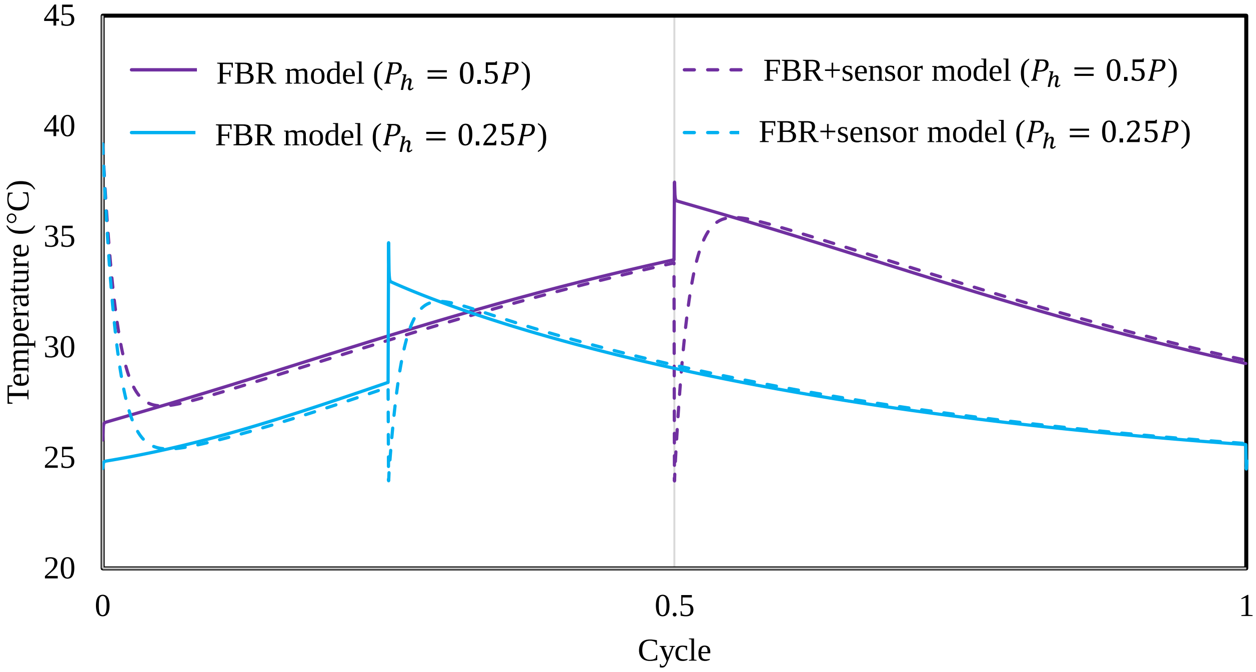

Figure 20: Air temperature profile from the FBR model and the combined FBR and sensor model for the equal and unequal hot and cold period duration at 120s cycle duration (NTU=2.4, face velocity=2.0 m/s, a time constant =1.5 s)

Figure 21 shows the comparison of the effectiveness errors for equal and unequal periods at different cycle durations. Compared to the equal period, the magnitude of effectiveness error (due to the transient response of sensors to temperature change) increases for the exchanger sensor, while it decreases for the duct sensor during an unequal period. At the operating conditions considered in this study, the exchanger sensors overestimate the effectiveness for the equal and unequal period by a maximum of about 8% and 16% (at a cycle time of 15 seconds), respectively. On the other hand, the duct sensor's corresponding maximum effectiveness errors are 12% and 10.5% for equal and unequal periods, respectively.

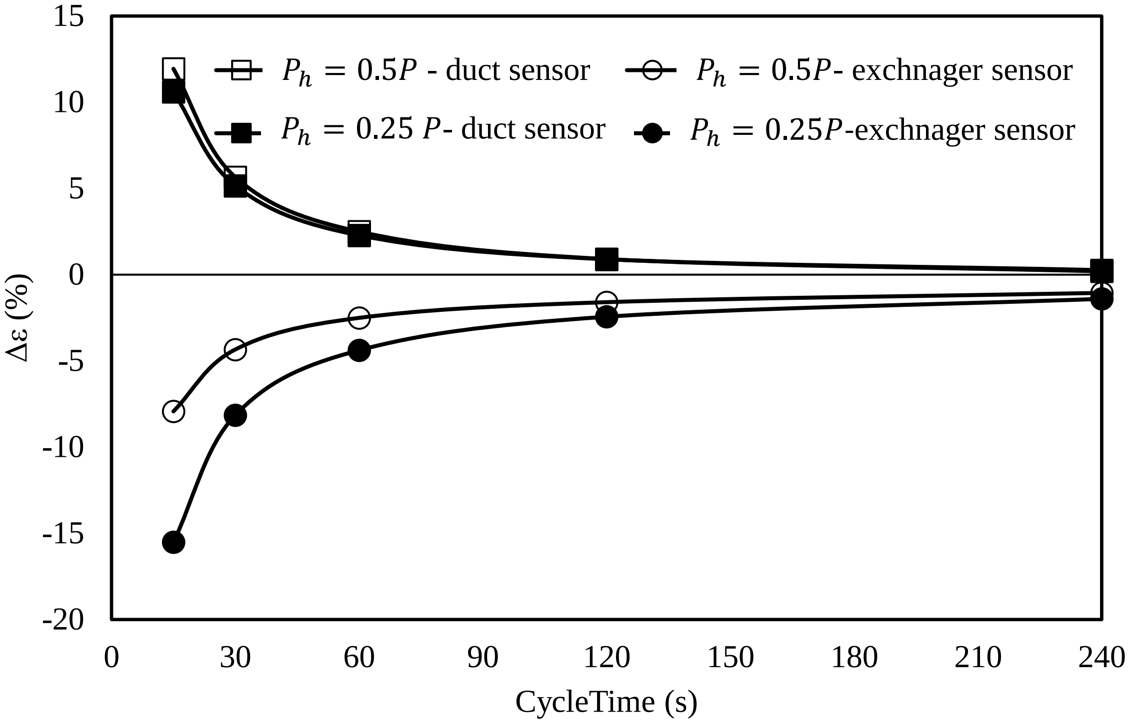

Figure 21: Comparison of effectiveness error (Δε) of equal and unequal heating and cooling duration for the duct and exchanger sensors at the different cycle times ((NTU=2.4, face velocity=2.0 m/s, a time constant =1.5 s)

5 Conclusions

In this paper, a 1-D numerical model, consisting of an exchanger (FBR) model and sensor model, to evaluate the performance of FBRs and to capture the transient nature of FBRs has been developed and validated. The exchanger (FBR) model is validated against available correlations and data in literature over a wide range of design parameters (NTU_o and Cr* and longitudinal conduction parameter (λ)). In addition, since experimental measurements include sensor transients' response, the experimental data from a small-scale test facility are used to validate the combined FBR and sensor model for both the initial transient and the quasi-steady-state operation of FBRs. The numerical model is capable of predicting the effectiveness error due to the sensor response to the transient temperature of FBRs. The "effectiveness error" is defined as the difference between the FBR (exchanger) model's effectiveness and the combined FBR and sensor model's effectiveness. It is found that the location of temperature sensors (i.e., either location, stationary (duct sensors), or attached to the moving exchanger (exchanger sensors)), affects the temperature profile and the effectiveness error. The duct sensors underestimate the effectiveness, while the exchanger sensors overestimate the effectiveness of FBRs.

As an application of the presented model, the temperature profile and effectiveness errors are obtained for several operating conditions of FBRs for HVAC applications. The conditions include a balanced/unbalanced flowrate FBRs and equal/unequal heating and cooling periods. For the balanced flow conditions, the maximum effectiveness error is around 10% for sensors with a time constant of 1.5 s and a cycle time of 15 s—the effectiveness error increases (maximum 15%) for unbalanced FBRs. For the unequal heating and cooling periods (balanced flow rate), the effectiveness errors from the duct sensor are close to the equal periods (maximum of 11%). In contrast, the exchanger sensors (with a time constant 1.5 s) overestimate the effectiveness by a maximum of 16% compared to 8% (at a cycle time of 15 s) for the equal heating/cooling period duration.

ACKNOWLEDGMENTS

Financial support from the College of Engineering and the College of Graduate and Postdoctoral Studies of the University of Saskatchewan, National Science and Engineering Research Council (NSERC), Canada and Tempeff North America Inc., Winnipeg, Canada (Project No: 533225-18) are much appreciated.

References

[1] M.I. Nizovtsev, V.Y. Borodulin, V.N. Letushko, A.A. Zakharov, Analysis of the efficiency of air-to-air heat exchanger with a periodic change in the flow direction, Appl. Therm. Eng. 93 (2016) 113–121. https://doi.org/10.1016/j.applthermaleng.2015.09.029.

[2] M. Justo Alonso, P. Liu, H.M. Mathisen, G. Ge, C. Simonson, Review of heat/energy recovery exchangers for use in ZEBs in cold climate countries, Build. Environ. 84 (2015) 228–237. https://doi.org/10.1016/J.BUILDENV.2014.11.014.

[3] H. Klein, S.A. Klein, J.W. Mitchell, Analysis of regenerative enthalpy exchangers, Int. J. Heat Mass Transf. 33 (1990) 735–744. https://doi.org/10.1016/0017-9310(90)90171-P.

[4] F. Kreith, E.E. Michaelides, CRC Handbook of Thermal Engineering, Second Edi, Taylor & Francis, CRC Press, Boca Raton, 2018.

[5] A.A. Rabah, A. Fekete, S. Kabelac, Experimental investigation on a rotary regenerator operating at low temperatures, J. Therm. Sci. Eng. Appl. 1 (2009) 1–9. https://doi.org/10.1115/1.4001543.

[6] J. Seo, D. Lee, D. Kim, International Journal of Heat and Mass Transfer A simple effectiveness model for heat wheels, Int. J. Heat Mass Transf. 120 (2018) 1358–1364. https://doi.org/10.1016/j.ijheatmasstransfer.2017.12.102.

[7] F. Fathieh, R.W. Besant, R.W. Evitts, C.J. Simonson, Determination of air-to-air heat wheel sensible effectiveness using temperature step change data, Int. J. Heat Mass Transf. 87 (2015) 312–326. https://doi.org/10.1016/j.ijheatmasstransfer.2015.04.028.

[8] F. Fathieh, A Novel Transient Testing Method for Heat/Energy Wheel Components, University of Saskatchewan, 2016.

[9] H. Ramin, E.N. Krishnan, A. Gurubalan, W.O. Alabi, C.J. Simonson, Transient sensor errors and their impact on fixed-bed regenerator (FBR) testing standards, Sci. Technol. Built Environ. 0 (2020) 1–22. https://doi.org/10.1080/23744731.2020.1846428.

[10] H. Jouhara, N. Khordehgah, S. Almahmoud, B. Delpech, A. Chauhan, S.A. Tassou, Waste heat recovery technologies and applications, Therm. Sci. Eng. Prog. 6 (2018) 268–289.

https://doi.org/10.1016/j.tsep.2018.04.017.

[11] T. Skiepko, R.K. Shah, Modeling and effect of leakages on heat transfer performance of fixed matrix regenerators, Int. J. Heat Mass Transf. 48 (2005) 1608–1632. https://doi.org/10.1016/j.ijheatmasstransfer.2004.10.023.

[12] M.T. Zarrinehkafsh, S.M. Sadrameli, Simulation of fixed bed regenerative heat exchangers for flue gas heat recovery, Appl. Therm. Eng. 24 (2004) 373–382. https://doi.org/10.1016/j.applthermaleng.2003.08.005.

[13] Y. Reboussin, J.F. Fourmigué, P. Marty, O. Citti, A numerical approach for the study of glass furnace regenerators, Appl. Therm. Eng. 25 (2005) 2299–2320. https://doi.org/10.1016/j.applthermaleng.2004.12.012.

[14] H. Ramin, E.N. Krishnan, C.J. Simonson, Fixed bed regenerators for HVAC applications, 27th Can. Congr. Appl. Mech. (2019) 1–6. https://doi.org/10.3390/proceedings2019023004.

[15] C.C. Chang, J. De Liang, S.L. Chen, Performance investigation of regenerative total heat exchanger with periodic flow, Appl. Therm. Eng. 130 (2018) 1319–1327. https://doi.org/10.1016/j.applthermaleng.2017.11.024.

[16] V.Y. Borodulin, M.I. Nizovtsev, A criterial analysis of the effectiveness of air-to-air heat exchangers with periodic change of airflow direction, Appl. Therm. Eng. 130 (2018) 1246–1255. https://doi.org/10.1016/j.applthermaleng.2017.11.126.

[17] Y.I. Aristov, I.V. Mezentsev, V.A. Mukhin, A new approach to regenerating heat and moisture in ventilation systems, Energy Build. 40 (2008) 204–208. https://doi.org/10.1016/J.ENBUILD.2007.02.029.

[18] M.I. Nizovtsev, V.Y. Borodulin, V.N. Letushko, Influence of condensation on the efficiency of regenerative heat exchanger for ventilation, Appl. Therm. Eng. 111 (2017) 997–1007. https://doi.org/10.1016/j.applthermaleng.2016.10.016.

[19] Heat Recovery System | Heat Recovery Ventilator | ERV | Energy Recovery, (n.d.). https://www.tempeffnorthamerica.com/ (accessed January 6, 2020).

[20] E.N. Krishnan, H. Ramin, M. Shakouri, L.D. Wilson, C.J. Simonson, Development of a small-scale test facility for effectiveness evaluation of fixed-bed regenerators, Appl. Therm. Eng. 174 (2020) 115263. https://doi.org/10.1016/j.applthermaleng.2020.115263.

[21] C. Eduardo, L. Nóbrega, Desiccant-Assisted Cooling Fundamentals and Applications, Springer, New York, 2014.

[22] R.K. Shah, D.P. Sekulic, Fundamentals of heat exchanger design, New Jersey, 2004. https://doi.org/10.1007/bf00740254.

[23] H. Ramin, E.N. Krishnan, G. Annadurai, C.J. Simonson, Transient performance of fixed-bed regenerators for energy recovery in building applications, in: Proc. ASME 2020 Heat Transf. Summer Conf. HT2020, ASME, Orlando, Florida, 2020.

[24] H. Ramin, E.N. Krishnan, W. Alabi, C.J. Simonson, Temperature Measurement Correction for the Determination of the Effectiveness of Fixed-Bed Regenerators (FBRs) for HVAC Applications, in: 2020 ASHRAE Annu. Summer Conf., ASHRAE, Austin, 2020.

[25] H. Hausen, Heat Transfer in Counterflow, Parallel Flow and Cross Flow, McGraw-Hill, Inc, New York, 1983.

[26] T.L. Bergman, A.S. Lavine, F.P. Incropera, D.P. Dewitt, Fundamentals of heat and mass transfer, Seventh e, John Wiley & Sons, INC., 2011.

[27] C.J. Simonson, R.W. Besant, Energy wheel effectiveness: Part I-development of dimensionless groups, Int. J. Heat Mass Transf. 42 (1999) 2161–2170. https://doi.org/10.1016/S0017-9310(98)00325-1.

[28] C.J. Simonson, R.W. Besant, Heat and moisture transfer in desiccant coated rotary energy exchangers: Part I - numerical model, ASHRAE Trans. 104 (1998) 229. https://doi.org/10.1080/10789669.1997.10391382.

[29] W. Shang, R.W. Besant, Theoretical and experimental methods for the sensible effectiveness of Air-to-Air energy recovery wheels, HVAC R Res. 14 (2008) 373–396. https://doi.org/10.1080/10789669.2008.10391015.

[30] R.K. Shah, A.L. London, Laminar Flow Forced Convection In Ducts, ACADEMIC PRESS, London, 1978.

[31] CSA Group, CSA C439 Laboratory methods of test for rating the performance of heat / energy-recovery, CSA Group, 2018.

[32] ASHRAE, BSR/ASHRAE Standard 84-2013R, Method of Testing Air-to-Air Heat/Energy Exchangers (First Public Review Draft), Atlanta, 2019.

[33] H. Versteeg, W. Malalasekera, An Introduction to Computational Fluid Dynamics, The Finite Volume Method, Pearson Education Limited, 2007. https://doi.org/10.2514/1.22547.

[34] C.J. Simonson, Heat and moisture transfer in energy wheels, University of Saskatchewan, 1998.

[35] G.D. Bahnke, C.P. Howard, The effect of longitudinal heat conduction on

periodic-flow heat exchanger performance, J. Eng. Gas Turbines Power. 86 (1964) 105–117. https://doi.org/10.1115/1.3677551.

[36] R.K. Shah, A Correlation for Longitudinal Heat Conduction Effects in Periodic-Flow Heat Exchangers, J. Eng. Powerngineering Power. (1975) 453–454.

[37] O. Buyukalaca, T. Yilmaz, Influence of rotational speed on effectiveness of rotary-type heat exchanger, Heat Mass Transf. 38 (2002) 441–447. https://doi.org/DOI 10.1007/s002310100277.

[38] E. Krishnan, H. Ramin, C.J. Simonson, Performance testing of fixed-bed regenerators for hvac applications, in: Second Pacific Rim Therm. Eng. Conf., Hawaii, 2019: pp. 1–5.